Heliyon 10 (2024) e30651

Contents lists available at ScienceDirect

Heliyon

journal homepage: www.cell.com/heliyon

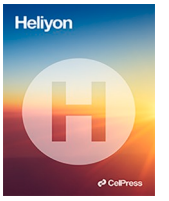

Research article

Stacking learning based on micro-CT radiomics for outcome prediction in the early-stage of silica-induced pulmonary fibrosis model

Hongwei Wang [a,b,1], Qiyue Jia [a,b,1], Yan Wang [a,b], Wenming Xue [a,b], Qiyue Jiang [a,b], Fuao Ning [a,b], Jiaxin Wang [a,b], Zhonghui Zhu [a,b,**], Lin Tian [a,b,*]

[a] Department of Occupational and Environmental Health, School of Public Health, Capital Medical University, Beijing, 100069, China
[b] Beijing Key Laboratory of Environmental Toxicology, Capital Medical University, Beijing, 100069, China

ARTICLE INFO

Keywords:
Silicosis
Micro-CT
Densitometric biomarkers
Non-aerated volume
Stacking learning

ABSTRACT

Silicosis is a progressive pulmonary fibrosis disease caused by long-term inhalation of silica. The early diagnosis and timely implementation of intervention measures are crucial in preventing silicosis deterioration further. However, the lack of screening and diagnostic measures for early-stage silicosis remains a significant challenge. In this study, silicosis models of varying severity were established through a single exposure to silica with different doses (2.5mg/mice or 5mg/mice) and durations (4 weeks or 12 weeks). The diagnostic performance of computed tomography (CT) quantitative analysis was assessed using lung density biomarkers and the lung density distribution histogram, with a particular focus on non-aerated lung volume. Subsequently, we developed and evaluated a stacking learning model for early diagnosis of silicosis after extracting and selecting features from CT images. The CT quantitative analysis reveals that while the lung densitometric biomarkers and lung density distribution histogram, as traditional indicators, effectively differentiate severe fibrosis models, they are unable to distinguish early-stage silicosis. Furthermore, these findings remained consistent even when employing non-aerated areas, which is a more sensitive indicator. By establishing a radiomics stacking learning model based on non-aerated areas, we can achieve remarkable diagnostic performance to distinguish early-stage silicosis, which can provide a valuable tool for clinical assistant diagnosis. This study reveals the potential of using non-aerated lung areas as a region of interest in stacking learning for early diagnosis of silicosis, providing new insights into early detection of this disease.

1. Introduction

Silicosis, a disease characterized by pulmonary fibrosis resulting from prolonged inhalation of respirable crystalline silica, is

* Corresponding author. Department of Occupational and Environmental Health, School of Public Health, Capital Medical University, No. 10, Xitoutiao Youanmen Street, Beijing, 100069, China.
** Corresponding author. Department of Occupational and Environmental Health, School of Public Health, Capital Medical University, No. 10, Xitoutiao Youanmen Street, Beijing, 100069, China.
E-mail addresses: zhuzhonghui@163.com (Z. Zhu), tian_lin@163.com (L. Tian).
[1] These authors contributed equally to this work.

https://doi.org/10.1016/j.heliyon.2024.e30651
Received 16 November 2023; Received in revised form 28 February 2024; Accepted 1 May 2024
Available online 6 May 2024

increasingly prevalent in both developing and developed countries. This poses a global public health challenge due to the emergence of contemporary industries such as sandblasting denim, stone fabrication, and jewelry polishing [1,2]. Due to the unclear pathogenesis, there is a lack of effective early diagnosis and treatment methods, which urgently necessitates early diagnosis and clinical interventions to alleviate disease progression and reduce mortality rates associated with advanced silicosis [3,4].

According to the current guidelines of the International Labour Organization, the primary approach for diagnosing silicosis involves analyzing chest X-ray and considering a history of occupational exposure to silica dust. Therefore, chest X-rays serve as the principal radiological diagnostic method [4,5]. The sensitivity of chest X-ray increases with the severity of silicosis; however, in preclinical and mild cases, the diagnostic effectiveness of chest X-ray is compromised due to its limited ability to accurately assess small shadows and early manifestations of parenchymal lesions [6]. The application of CT has enhanced the noninvasive diagnostic approach for qualitative and quantitative assessment of various pulmonary diseases, thereby providing a more comprehensive and precise depiction of pathological conditions. Therefore, the utilization of CT instead of chest X-ray in the screening and early diagnosis of pneumoconiosis holds a significant implication for future advancements [7–9].

However, in most cases, CT is still not implemented in population screening and early diagnosis due to the requirement for professional and experienced analysts to perform manual image analysis and diagnosis. Despite the experienced radiographers, there is still variability in the interpretation of CT scans for silicosis diagnosis, both within individuals and among different radiographers, which could hinder further application of CT in silicosis diagnosis [10,11]. In recent years, addressing these challenges has prompted the research focused on early diagnosis and clinical treatment research: quantitative analysis of CT imaging or the application of machine learning for medical imaging-aided diagnosis [12–14]. This approach offers a novel strategy characterized by its rapid speed, high accuracy, broad applicability, and strong repeatability compared to visual assessment. For instance, some densitometric parameters have been utilized in the diagnosis of pulmonary diseases [14,15]. The utilization of CT-derived densitometric biomarkers allows for the assessment of inflammation and non-resolving fibrosis in a sensitive and non-invasive manner [16]. The latest research has developed a CSNet model based on HRCT [11], presenting a novel approach for medical imaging-aided diagnosis of pneumoconiosis patients. Although CT has the potential to achieve the diagnosis of silicosis at an early stage or even earlier, since it is more sensitive than chest X-ray in detecting emphysema, early parenchymal changes, and pleural thickening [17], relevant research has not yet been undertaken at present, which could do more for the health of those exposed.

The diagnostic capability of CT-derived densitometric biomarkers for the multiple dose silica-induced fibrosis model was assessed in this study. We found that the detection of early-stage silicosis is undistinguishable through the quantitative analysis of CT imaging. Consequently, machine learning is employed to further this work. Ultimately, the stacking ensemble learning analysis strategy is utilized to yield more precise and consistent evaluation outcomes. The objective of this study is to establish an assessment tool for the timely detection of silicosis in the early stage, which can facilitate early screening and clinical diagnosis.

2. Materials and methods

2.1. Experimental animal models

35 male C57BL/6J mice were purchased from Vital River Laboratory Animal Technology Co. Ltd. (Beijing, China). They were 8 weeks and weight weighed 20–22 g. The mice were housed in specific pathogen-free conditions, with free access to food and water. The ambient temperature is controlled at 24 °C ± 1 °C, with a 12-h light-dark cycle. After a week of adaptive feeding, mice were randomly divided into 5 groups: 2.5 mg silica treated for 4 weeks(4W_S); 5 mg silica treated for 4 weeks(4W_2S), and the same batch control for 4 weeks (4W_C); 5 mg silica treated for 12 weeks(12W_2S) and it's corresponding control(12W_C). Mice in 4W_S, 4W_2S and 12W_2S groups were instilled with 2.5 mg, 5 mg and 5 mg silica (Sigma Aldrich, USA) in 50 μL saline, respectively, the same batch controls (4W_C and 12W_C) were instilled with an equal volume of saline. The intratracheal instillation was carried out only once at the beginning of 4 weeks or 12 weeks before micro-CT acquisition.

2.2. Micro-CT acquisition protocol

The micro-computed tomography (Micro-CT) scan was carried out on 4 and 12 weeks after silica exposure by Skyscan 1276 (Bruker, Germany). The mice were deprived of forage the night before the experiment.

The mice were anesthetized using a 4 % isoflurane in an oxygen/air mixture delivered through the R500 small animal anesthesia machine (RAD, China). Subsequently, the anesthetized mice were positioned supine on the scanner bed with an anesthetic mask to maintain anesthesia at 2 % isoflurane concentration, and the thoracic region was delineated for scanning. Images were acquired with the following parameters: X-ray tube voltage 70 kV, X-ray tube current 200 μA combined with a composite X-ray filter of 0.5 mm aluminum, 137 ms exposure time per projection, acquiring projections with 0.5° rotation step. Image pixel size was 35 μm and scanning took approximately 8 min for each mouse. We use ddH_2O for Hounsfield unit (HU) calibration, the water was set at 0 HU and the air at − 1000 HU. Each mouse we got about 520 images from the software provided by Bruker.

We used the Mimics Research 20.0 software (Materialise, Belgium) for the 3D reconstruction and visualization, used the threshold and region grow tools to segment the lung from the body, the threshold used to distinguish aerated and non-aerated lung volume was set at −185 HU, where the main contours of the lung can be distinguished from the surrounding tissue and similar to that of Bert's [18]. Manually delineation was applied to segment the ambiguous boundaries due to severe fibrosis when necessary [19]. The threshold to distinguish Hyper-inflated and Normo-aerated volume was set at −700 HU, which made the outline of the trachea visible. For the quantification of the lung density, we exported the lung mask from Mimics Research and applied the mask to the CT images in CTAn

software (Bruker, Germany).

2.3. H&E and Masson staining

The lung tissue of mice was soaked in 4 % polyformaldehyde (Biosharp, China) for 24h, the lung was cut into 5-μm thick slices after paraffin embedding. The slices were stained with hematoxylin and eosin(H&E) as well as Masson. Using the Pannoramic SCAN II (3D-Histech, Hungary) to scan glass slices into full-field images. The sections were observed with CaseViewer software (3D-Histech, Hungary) with 100 × or 200 × magnification.

2.4. CT images feature extraction and selection

Non-aerated lung volume is a sensitive index for indication of pulmonary fibrosis. The part of the whole lung mask with HU > -185 is considered as the non-aerated area. We selected one slice every five layers from the fifth to the seventh vertebra, and 20 slices per mouse were obtained to guarantee stability and representativeness [20]. We obtained 220 control and 300 silica slices by the above method. The non-aerated area is applied to the corresponding lung slice as the region of interest (ROI). In Python, 120 features were extracted via Pyradiomics (version 3.1.0), an open-source toolbox. To reduce overfitting and redundancy in radiomics analysis, feature selection was necessary. LASSO was applied in the training set for dimensionality reduction and feature selection [21], and the prediction accuracy and interpretability of the statistical model were able to enhanced after performing this variable selection and regularization. Fivefold cross-validation was applied for tuning parameter(λ) selection in the LASSO via the minimum criterion and the features with non-zero coefficients were selected.

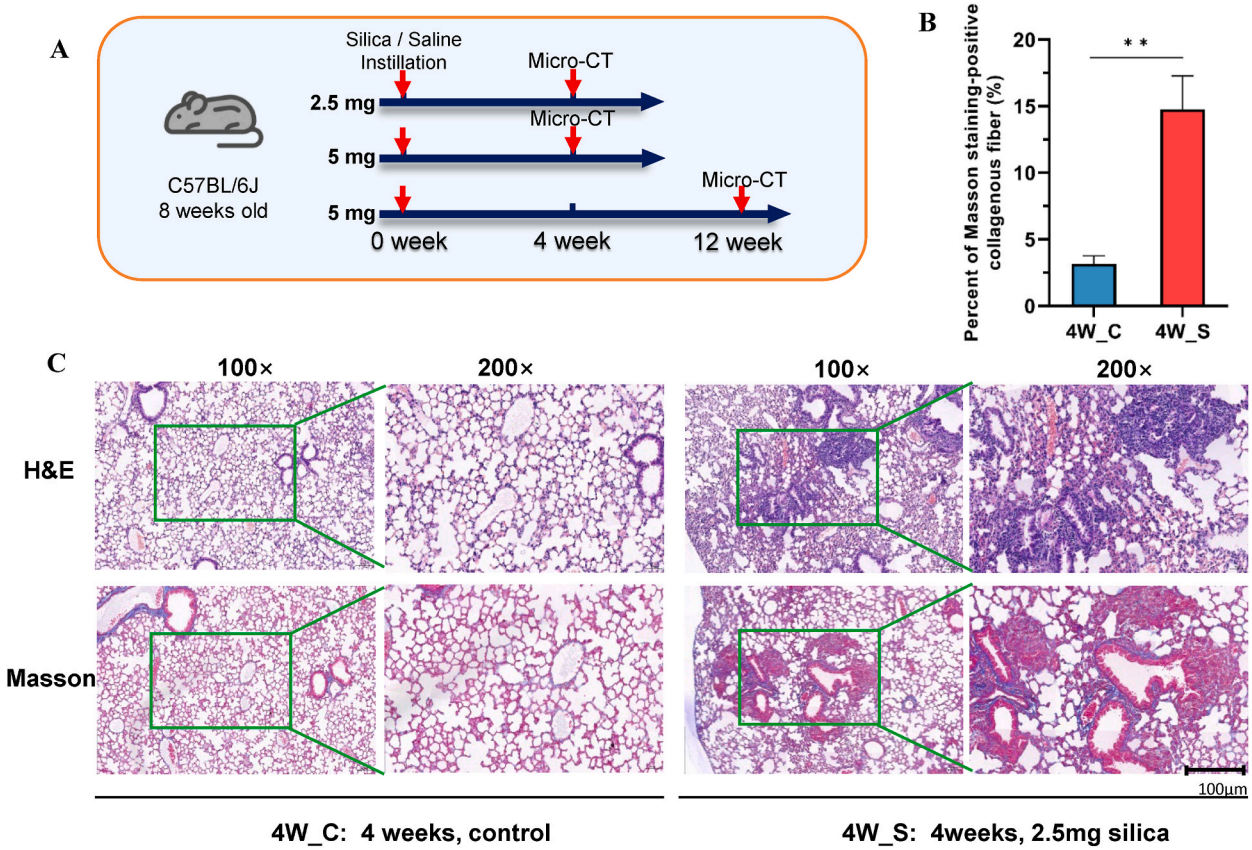

Fig. 1. Successful establishment of animal silicosis model
(A). Procedure for experimentation, the CT acquisition was performed at 4 or 12 weeks after exposure.
(B). Percent of Masson staining-positive collagenous fiber, the blue staining area of 4W_S was significantly increased. Data were shown as mean ± standard error of the mean (SEM) and assessed with One-way ANOVA test. n = 5, $^{**}p < 0.01$.
(C). H&E and Masson staining slices in 4W_C and 4W_S. A significant infiltration of inflammatory cells within the pulmonary interstitial, accompanied by a distinct formation of silicotic nodules around the trachea and vascular bed in H&E and increased blue-stained collagen fibers in Masson can be found in 4W_S. (For interpretation of the references to colour in this figure legend, the reader is referred to the Web version of this article.)

2.5. Development and evaluation of the deep learning model

We tested and compared the performance of six machine learning classifiers as base models [22], Logistic Regression (LR), Support Vector Machine (SVM), Gaussian Naïve Bayes (GNB), Decision Tree (DT), K-nearest Neighbor (KNN) and Multilayer Perceptron (MLP). The training and testing sets were automatically split in a 7:3 ratio and the performance of six classifiers was evaluated and compared on the basis of the Area Under Curve (AUC) value with fivefold cross-validation. The stacking model utilizing the soft voting mechanism was executed subsequent to the completion of the six base models [23]. In this study, Catboost, LR, Random Forest and XGBoost were evaluated with five splits of the five-fold cross-validation approach and the feature selection was re-executed utilizing LR as the ultimate model.

2.6. Statistical analysis

SPSS Statistics 23.0 software (IBM, USA) was performed for statistical analysis. We presented all data as Mean ± Standard Error of Mean (SEM). The one-way analysis of variance (ANOVA) was applied to multiple-group comparisons. Where differences were identified ($p < 0.05$), a Dunnett's or Dunn's multiple comparison post hoc test was performed. Images were generated using GraphPad Prism 9(GraphPad Software, USA) and OriginPro 2023(OriginLab Corporation, USA).

3. Results

3.1. Pathological changes in the lungs of mice instilled with silica

The mice were instilled with 2.5 or 5 mg silica and the CT acquisition was performed at 4 or 12 weeks after exposure (Fig. 1A). The histopathological section was examined to assess tissue morphology and pathology, confirming the successful establishment of the animal model. We found distorted lung morphologies in the group exposed to 2.5 mg of silica for 4 weeks (4W_S), this dose was used to simulate early-stage silicosis and has been employed in multiple studies [24–27], characterized by alveolar wall thickening and collapse compared to control(4W_C). H&E staining revealed a significant infiltration of inflammatory cells within the pulmonary interstitial, accompanied by a distinct formation of silicotic nodules around the trachea and vascular bed (Fig. 1C). Corresponding

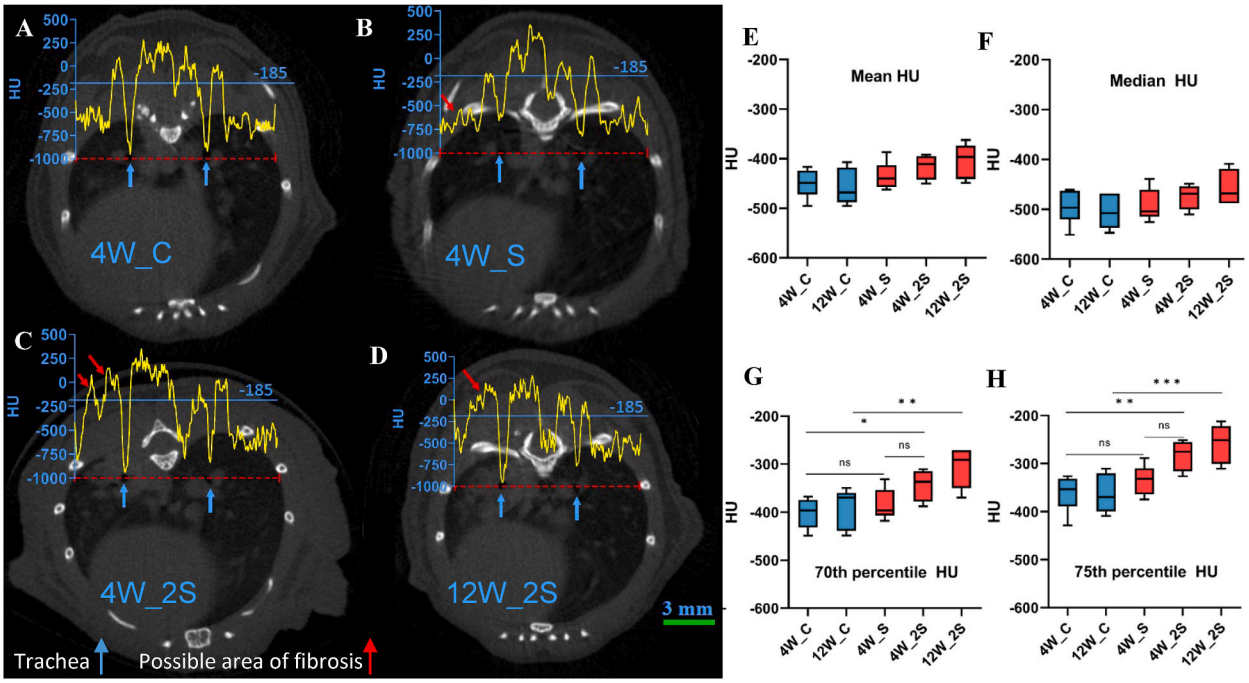

Fig. 2. Analysis from the CT slices and Lung densitometric biomarkers results
(A-D). Typical CT slices show that 4W_S (B) has almost ignorable visibility of fibrosis, while the 5 mg group was significantly aggravated at 4 weeks (C) and 12 weeks (D).
(E–H). Whole lung densitometric biomarkers such as Mean (E), Median (F), 70th percentile (G) and 75th percentile (H) of HU computed in all layers' area of the lung, in the control (blue) and silica(red) group. 4W_S is indistinguishable by lung densitometric biomarkers while 4W_2S and 12W_2S are distinguishable.
Data were shown as mean ± SEM and assessed with One-way ANOVA test. n ≥ 4, $^{ns}p \geq 0.05$, $^{*}p < 0.05$, $^{**}p < 0.01$, $^{***}p < 0.001$. (For interpretation of the references to colour in this figure legend, the reader is referred to the Web version of this article.)

Masson's staining exhibited a prominent deposition of blue-stained collagen fibers within the pulmonary interstitial and the silicotic nodules (Fig. 1B–C).

3.2. Early-stage silicosis is indistinguishable by lung densitometric biomarkers

To assess the efficacy of micro-CT in characterizing silica-induced pulmonary fibrosis, we conducted HU analysis on CT slices. The non-aerated areas refer to the portion with HU above −185 which may indicate blood vessels or lung areas characterized by heightened density due to fibrosis. However, despite morphological changes, micro-CT cannot distinguish the silicosis in the early stage (Fig. 2B).

Then our study used increasing doses (5 mg for 4 weeks, 4W_2S) and prolonging duration (5 mg for 12 weeks, 12W_2S) of the disease as positive controls. We found these high-dose groups and prolonging durations (Fig. 2C–D) exhibited significantly heightened density on CT slices. This high-density pattern undergoes a transition to a continuous form in Fig. 2D at 12W_4S, indicating a further deterioration of the condition.

Based on the HU, we employed a semi-automatic method to segment the whole lung and computed the lung densitometric biomarkers. The mean (Fig. 2 E), median (Fig. 2 F), 70th percentile (Fig. 2 G), and 75th percentile (Fig. 2 H) lung density increased in the

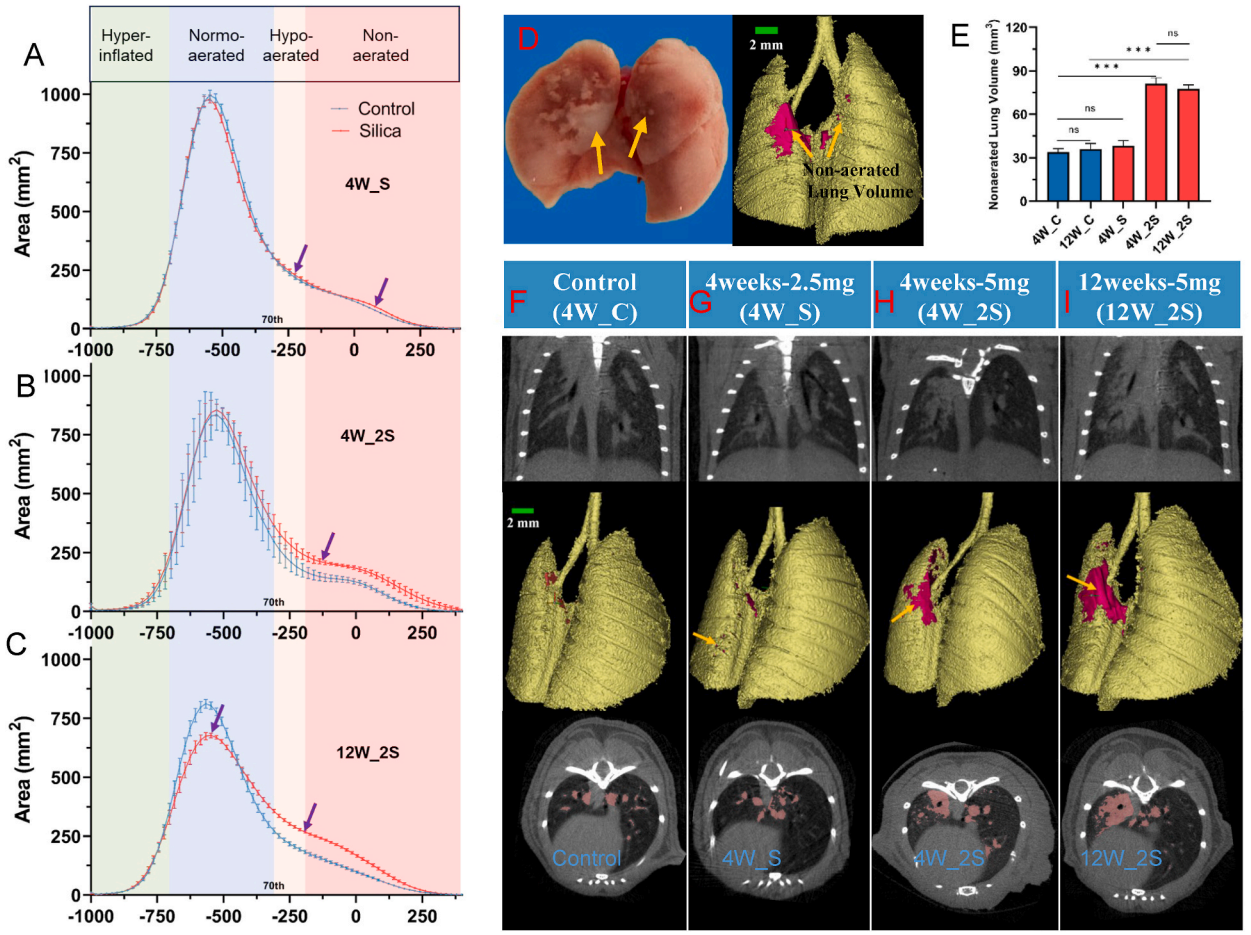

Fig. 3. Lung density distribute histogram analysis(A-C) and non-aerated lung volume analysis(D-I)
(A–C). Lung density distributes histogram analysis in 4W_C vs. 4W_S (A), 4W_C vs. 4W_2S(B), 12W_C vs. 12W_2S(C) The lung aeration compartments were defined by the following HU ranges: in light green the hyper-inflated [−1024, −700] HU, in light blue the normo-aerated [−700, −310] HU, in light orange the hypo-aerated [-310, −185] HU and in light red the non-aerated [−185, +400] HU. Potential lesions or changes are indicated by purple arrows, with the blue line for the control and the red line for the silica. Lung segmentation and 3D reconstruction based on Mimics research.
(D). Silicosis model biopsy corresponds with lung segmentation and reconstruction.
(E). Non-aerated lung volume by lung segmentation in groups of different severity.
(F–I). From the first to the third columns are coronal CT slices, corresponding 3D reconstruction and segmented non-aerated area in axial CT slices of four groups.
Data were shown as mean ± SEM and assessed with One-way ANOVA test. n = 3–5, ***$p < 0.001$. (For interpretation of the references to colour in this figure legend, the reader is referred to the Web version of this article.)

silica-induced lung fibrosis model. However, this phenomenon was observed only in high-dose groups and prolonged duration. None of these biomarkers showed any significant difference in response to early-stage silicosis (4W_S vs. 4W_C).

The application of lung density histogram and non-aerated lung volume proves ineffective in distinguishing early-stage silicosis.

Specifically, 4W_S shows no discernible difference through lung densitometric biomarkers. Therefore, our goal is to fully utilize lung density information and identify a sensitive indicator.

We make a lung density distribution histogram in all layers' areas of the lung via CTAn. We set the interval [−1024, −700]HU as hyper-inflated lung volume and [−185, 400]HU as non-aerated volume as explained above. For normo-aerated and hypo-aerated lung volume, we referred to Laura et al. [19], 70th percentile of the area under the curve for the mice in control (blue line in Fig. 3A, n = 5) is included in the range [−1024, −310] HU. Additionally, the 70th percentile (Fig. 2G) shows a statistical difference between control and 4W/12W_2S. Excluding the hyper-inflated [−1024, −700]HU and non-aerated [−185, 400]HU volume, we defined the normo-aerated range as [−700, −310] HU and hypo-aerated range as [−310, −185] HU.

We found that there was an insignificant increase in the area, indicated by the purple arrows, in 4W_S compared to 4W_C (Fig. 3A) within the hypo-aerated and non-aerated volume ranges. However, the increase is more pronounced in 4W_2S (Fig. 3B) than in the same batch control, while this phenomenon is most obvious in 12W_2S (Fig. 3C). In addition, it was accompanied by a decline in the normo-aerated area in 12W_2S (Fig. 3C).

The utilization of CT enables the generation of images that can be subsequently utilized for the purpose of 3D reconstruction [28]. Here we used Mimics research software to segment and 3D reconstruct the lungs of mice, and the reconstructed non-aerated lung volumes (HU > -185) could visually reflect the biopsy, especially in the fibrosis areas(Fig. 3D). Non-aerated lung volume can indicate disease burden of fibrosis [16]. In fact, the 3D non-aerated lung volume is determined by overlaying the non-aerated areas on each CT section. The measurement of non-aerated lung volume has proven to be a highly sensitive and specific indicator [29], making it a valuable tool in numerous research studies [16,29]. As shown in Fig. 3E, the non-aerated lung volume didn't change between control

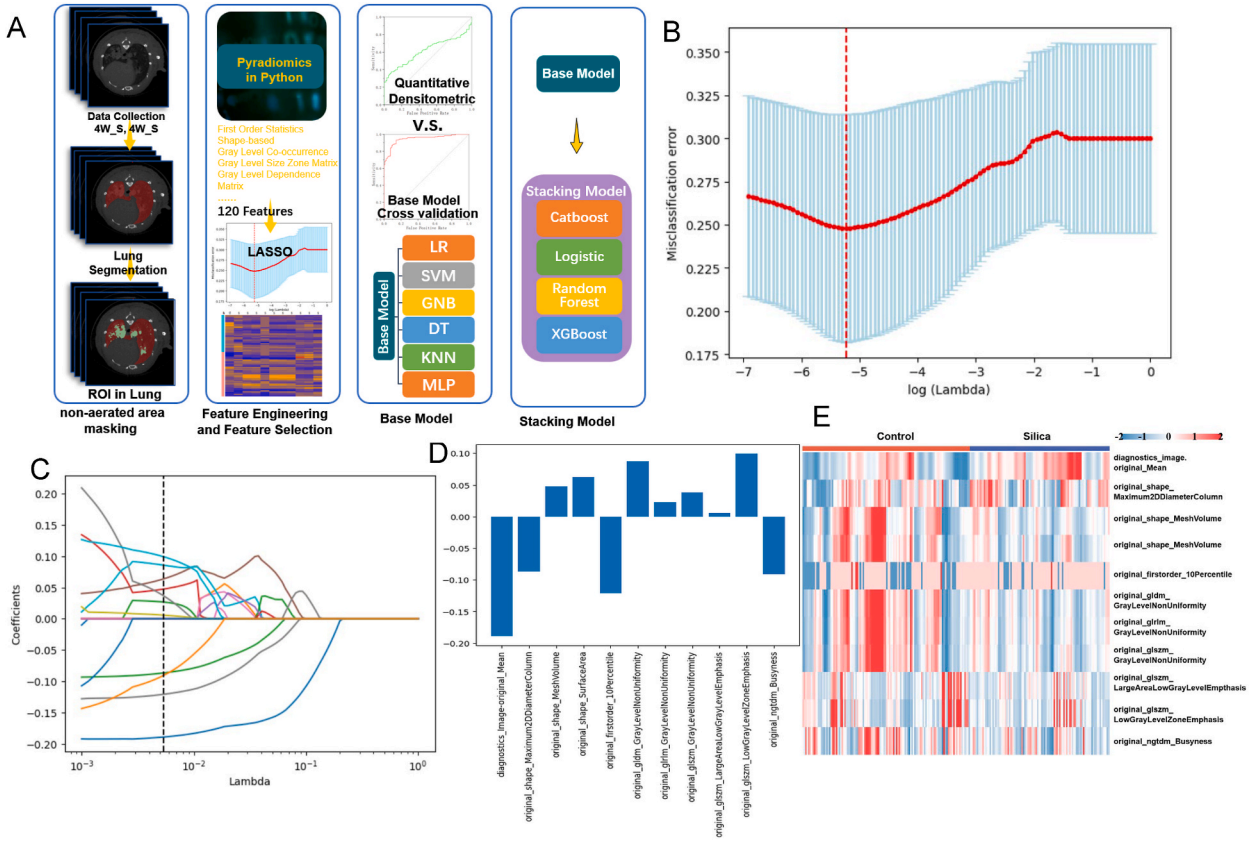

Fig. 4. Radiomics model establishment

(A). The model development workflow. The process of our model establishment includes the masking of non-aerated areas in the lung, feature extraction using the Pyradiomics package, feature selection with a LASSO, and basic model construction using the screened features. Ultimately, the stacking ensemble learning analysis strategy is utilized to yield more precise and consistent evaluation outcomes.

(B). Revealing the LASSO coefficient profiles of 11 radiomics characteristics.

(C). Selection of the tuning parameter (λ) in the LASSO model using the minimum criterion.

(D). Ultimately, a total of 11 features were selected.

(E). The clusters of slices with similar radiomics expression patterns.

in 4W_C compared to 12W_C. There is an upward trend between 4W_S and 4W_C, but no significant difference. The volumes in 4W_2S and 12W_2S are significantly increased than in the control, yet there is no difference between 4W_2S and 12W_2S. This indicates that the non-aerated lung volume exhibits a remarkable sensitivity compared to the whole lung densitometric biomarkers, such as median lung density.

The surface view of the non-aerated volume in control (Fig. 3F) was located near the pulmonary hilus, primarily consisting of blood vessels. The visibility between the 4W_S (Fig. 3G) CT slices and the surface view or segmented non-aerated area in axial CT slices compared to the control (Fig. 3F) was almost negligible. However, the lung surface is scattered with inconspicuous non-aerated spots on the 3D model. From 4W_2S (Fig. 3H) to 12W_2S (Fig. 3I), CT slices showed an aggravating trend, and the 3D model showed that the non-aerated volume extended to the lung surface.

3.3. *Stacking learning effectively identified early-stage silicosis*

Radiomics has the potential to capture nuanced variations in intensity and texture from images, while also enabling analysis of tissue attributes at a granular level. This approach may reveal additional characteristics that are not readily apparent in the original images [30]. Since densitometric biomarkers and non-aerated lung volume failed to provide a clear distinction for early-stage silicosis, we turned to radiomics.

The complete process flow is shown in Fig. 4A. Firstly, the process of our model establishment includes the masking of non-aerated areas in the lung. And then using the pyradiomics package in Python, all explanatory features were extracted from CT images. We performed the Radiomics features selection using the LASSO regression model. By tuning parameter (λ), the minimum criterion (represented by dotted vertical lines) was selected in the LASSO model and the value λ of 0.0053 was chosen (Fig. 4B). A coefficient profile plot was generated, eleven radiomics features with nonzero coefficients were ultimately selected (Fig. 4C). The selected

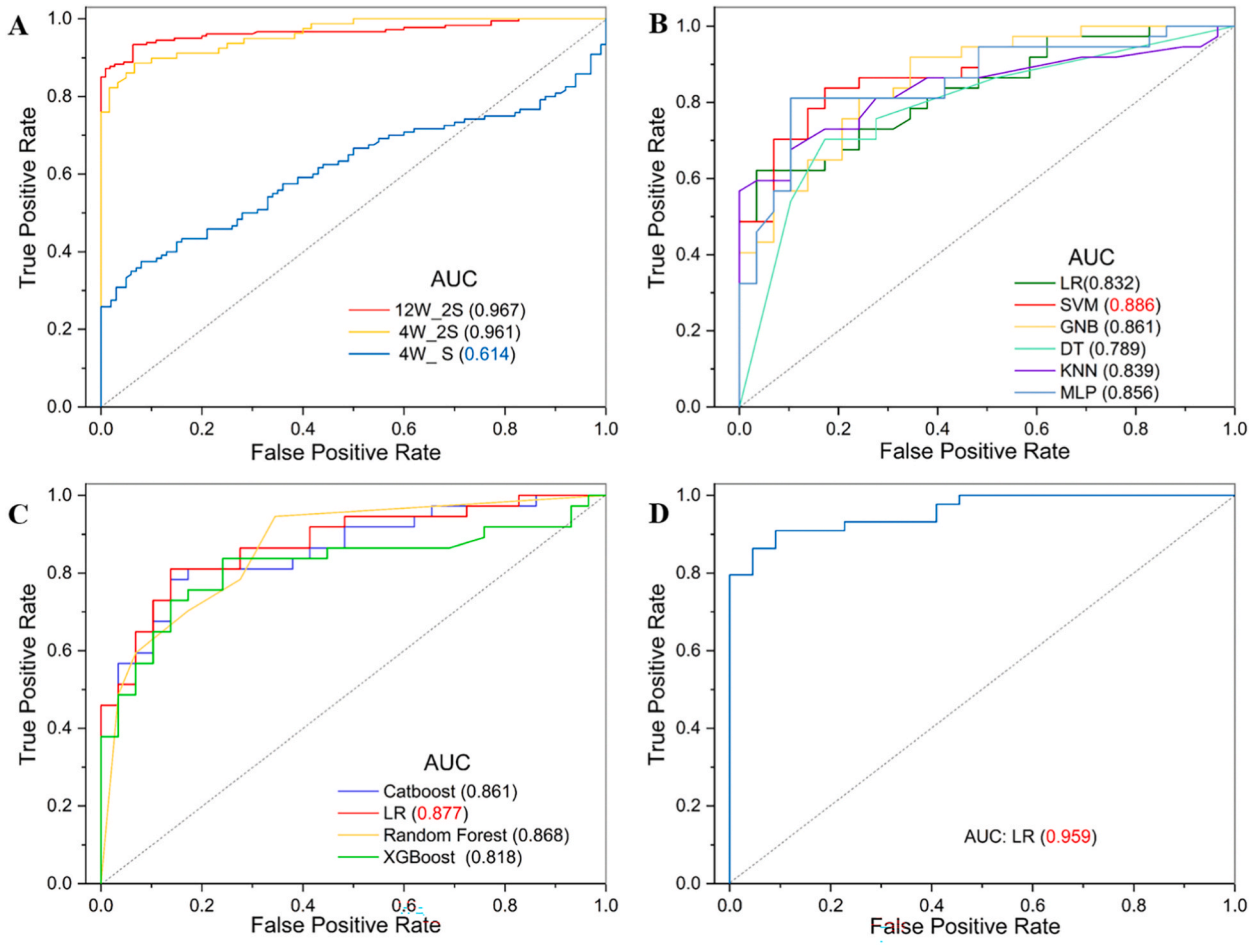

Fig. 5. The AUC curve before and after algorithm training
(A). The diagnostic capability of non-aerated lung areas and mouse models of different severity.
(B). Basic models were created using six different classifiers.
(C–D). The ROC curve of different stacking models(C) and ultimate model(D) in the testing set.

radiomics features are shown in (Fig. 4D). The heatmap (Fig. 4E) visually illustrates the clustering of all slices (n = 120) on the x axis and selected radiomics features (n = 11) on the y axis, indicated clusters of slices with similar radiomics expression patterns.

The statistical measure of AUC is widely used to evaluate classifier performance, offering a superior metric compared to accuracy [31]. Firstly, the AUC curve is made based on the non-aerated lung areas from original CT images (Fig. 5A). The results validated that the non-aerated lung area performs well in 4W_2S and 12W_2S. However, unsatisfactory performance in the 4W_S group, indicates that identifying low-dose silica-induced early-stage fibrosis by non-aerated lung area is indeed challenging.

Fig. 5B depicts the AUC curves of models created using six classifiers. The parameters of base classifiers were fine-tuned for optimal performance. The statistical results of five-fold cross-validation were applied to calculate the areas under the AUC curves. The AUC values of the classifiers were LR classifier 0.832 (0.732–0.932), Support Vector Machine (SVM) classifier 0.886 (0.806–0.966), Gaussian Naïve Bayes (GNB) classifier 0.861 (0.775–0.947), Decision Tree (DT) classifier 0.789 (0.675–0.904), K-nearest Neighbor (KNN) classifier 0.839 (0.732–0.945), and Multilayer Perceptron (MLP) classifier 0.856 (0.761–0.952).

The process of amalgamating multiple machine learning models into a unified prediction model [32], known as ensemble learning, is widely acknowledged as one of the foremost approaches for enhancing performance beyond individual models. The performance of the base model can be enhanced through the stacking model, one type of the ensemble learning model. Categorical boosting (Catboost), LR, Random Forest and eXtreme Gradient Boosting (XGBoost) were evaluated with five splits of the five-fold cross-validation approach. The results of the experiment are provided in Table 1, utilizing four metrics including accuracy, precision, recall rate, and F1 score, respectively. The stacking models in the training set demonstrated the following areas under the AUC curves: the Catboost model achieved an AUC of 0.861 (0.769–0.953), the LR model attained an AUC of 0.877 (0.791–0.963), the Random Forest model yielded AUCs of 0.868 (0.781–0.955), and XGBoost obtained an AUC of 0.818 (0.704–0.933). Lastly, within our dataset's training, we observed that the LR model obtained AUC values that were slightly greater than others. the feature selection was re-executed utilizing LR as the ultimate model resulting in the best performance.

4. Discussion

The global community continues to grapple with the formidable challenges posed by silicosis, particularly in countries such as Australia, India, China, and others. Timely diagnosis of this debilitating condition is essential for impeding its progression and enhancing patients' quality of life [33,34]. The widely utilized chest X-ray lacks the required sensitivity for early-stage silicosis diagnosis, whereas CT can compensate for this deficiency [7]. Currently, there are few studies on CT quantitative analysis for diagnosing early-stage silicosis. Our study suggests that CT density quantification and densitometric biomarkers are not sufficiently distinctive to differentiate the early-stage silicosis model. The subsequent step involved developing a stacking ensemble learning algorithm based on CT images, which enables accurate discrimination of early-stage silicosis. The diagnostic performance of all our algorithms surpassed that of CT density quantification. Among them, the SVM algorithm achieved a validation set accuracy of 0.886 and, through stacked learning, we further enhanced and integrated the AUC value of the final model to 0.959.

Lung density measurements, based on CT scans, reflect the degree of lung inflation and structural abnormalities. These can be characterized by decreased attenuation as observed in conditions like emphysema or cystic lung disease, or by increased attenuation as seen in pulmonary fibrosis [35]. The utilization of CT-based lung density measurements is deemed to be more objective and accurate compared to visual assessments and has been used in several pulmonary diseases [14,15,35]. Our study established silica-induced fibrosis models in mice using both high and low doses. The high-dose group received a dosage of 5 mg silica per mouse, consistent with peer studies that have demonstrated significant changes in CT imagines [16,36–38]. Meanwhile, the low dose group was administered a dosage of 2.5 mg silica per mouse via tracheal instillation. This dose was used to simulate early-stage silicosis and has been employed in multiple studies [24–27] due to its observable pathological alteration detectable by the naked eye. However, our study found that these lesions from low dose were not detectable through visual assessments of CT images. Based on the density measurement, we employed semi-automated techniques to segment the lung and compute four densitometric biomarkers such as average lung density. The higher rankings of these biomarkers indicate a greater sensitivity to characteristics of pulmonary fibrosis. The manifestation is specifically evident in the 4W_2S and 12W_2S, which showed only a slight increase in the mean and 50th percentile lung density. However, statistically significant differences were observed in the 70th and 75th, as these higher densities might better represent the fibrosis. Studies have reported that 70th can characterize the pathological status of pulmonary fibrosis [19], with values higher than this percentile defining the threshold for hypo-aerated lung areas. Similar to bleomycin-induced pulmonary fibrosis [39], our study revealed an increase in average lung density, median lung density, and the 70th and 75th percentiles in the silica-induced fibrosis model; however, these changes were observed only in the high-dose groups. Notably, after 12 weeks of exposure to 5 mg silica, the most significant elevation in lung density was observed. Unfortunately, our analysis of the low-dose group did not

Table 1
Performance of each model for stacking.

	Accuracy	Precision	recall	F1 Score
catboost	0.803	0.853	0.784	0.817
LR	0.818	0.857	0.811	0.833
Random Forest	0.773	0.839	0.703	0.765
xgboost	0.773	0.824	0.757	0.789
ultimate model	0.864	1.000	0.795	0.886

demonstrate satisfactory diagnostic efficacy. We only observed a trend of increased density at the 75th percentile, without a statistically significant difference.

To comprehensively characterize the lung's density composition, we generated a whole lung density attenuation histogram by threshold segmentation and categorized the whole lung density into four gradients: hyper-inflated lung area, normo-aerated area, hypo-aerated area and non-aerated area. We observed a marked elevation of hypo-aerated area and non-aerated area in the high-dose group compared to the control. This phenomenon was obviously at 12 weeks as opposed to 4 weeks. Furthermore, 12 weeks after exposure to 5 mg of silica, mice showed a significant decrease in normo-aerated area, indicating that the progressive nature of silicosis severely impairs lung function.

The non-aerated lung area, unlike the 70th percentile derived from the overall density distribution of the whole lung, specifically represents the unventilated portion of the lung and exhibits a remarkable sensitivity and specificity [29]. Several studies propose that non-aerated lung area can serve as an alternative non-invasive marker for assessing disease burden [16], including fibrosis and inflammatory response, and this parameter has been employed in various studies [16,29,40]. However, in the early-stage silicosis, there was no discernible increase observed in lung densitometric biomarkers, potential high-density areas in the lung density histogram, or 3D reconstruction based non-aerated area. Consequently, all these indicators were insufficient for reaching a definitive diagnostic conclusion.

The chronic and delayed-response nature of pulmonary fibrosis implies that the onset of fibrosis spans several weeks, with only minimal changes observed at earlier time points [41]. As a result, solely relying on density analysis of the entire lung might miss subtle pathological alterations, thereby hindering the ability to effectively monitor the nuanced lung density changes associated with pulmonary fibrosis through imaging quantitative analysis [42]. Although the non-aerated volume exhibits higher sensitivity than whole-lung densitometric biomarkers, distinguishing early-stage silicosis remains still challenging.

The application of radiomics enables the detection of subtle changes in intensity and texture within CT images, thereby revealing a broader spectrum of discernible features in the original image. This approach may offer valuable assistance in diagnosing early-stage silicosis. Therefore, we developed a diagnostic tool utilizing radiomics deep learning techniques. To ensure the efficacy of deep learning, we employed the 2D ROI from the segmented non-aerated area on each slice. One rationale behind this choice is that fibrosis may exist within the non-aerated areas in the lung. The non-aerated area, derived from threshold-based segmentation, reduces human subjectivity and eliminates the reliance on experts. While the 3D ROI outperforms the 2D, its intricate segmentation process is time-consuming, making it difficult to implement in clinical practice. In particular, 2D ROI calculations are simpler and less time-consuming [21]. Therefore, we chose to use the lamellar 2D ROI in CT scans as the database for our modeling. To ensure the selection of important and stable features in modeling, we applied LASSO regression and selected 11 features from 120 features. The diagnostic performance of machine learning depends on the selection of classifiers [43]. We tested six different types of classifiers: LR, SVM, GMB, DT, KNN, and MLP. The diagnostic performance of each classifier was higher than that of the AUC using the non-aerated lung area as the diagnostic criterion in the low-dose group. Notably, the SVM algorithm achieved the highest value in the validation set AUC, reaching 0.886.

The field of machine learning recognizes ensemble learning as the most advanced solution [10]. Stacking learning, a widely employed approach in ensemble learning constructs radiomics models that outperform those based on other individual machine learning classifiers [23]. Among the four stacked learning algorithms tested, the LR model exhibits several advantages including low complexity, making it suitable for linearly separable data, effectively avoiding overfitting, consuming minimal memory resources, and offering fast training speeds [44,45]. Most importantly, it demonstrates superior diagnostic efficiency. By implementing stacked learning, we refined and enhanced our model, achieving an AUC value of 0.959. This enabled us to develop a highly effective early diagnosis tool for silicosis. However, the present study still has certain limitations, particularly in terms of disparities between animal and human CT. Therefore, future investigations will utilize a human CT database to facilitate further analysis.

5. Conclusion

In conclusion, the present study investigated the efficacy of CT lung density measurements and non-aerated lung volume in the silicosis model, confirming the excellent diagnostic effectiveness of non-aerated lung volume. Given the challenges in distinguishing early silicosis, we established an evaluation tool using stacking learning with the non-aerated area as the ROI. This approach enhances the diagnostic efficiency of the early silicosis model and facilitates early screening and clinical diagnosis.

Ethics statement

This study was conducted according to the guidelines of the Declaration of Helsinki and approved by the Laboratory Animal Care and Use Committee at Capital Medical University in Beijing, China (AEEI-2018-223).

Funding statement

This study was supported by the National Natural Science Foundation of China (82073522, 82373545).

Data availability statement

The datasets used and/or analyzed during the current study are available from the corresponding author on reasonable request.

CRediT authorship contribution statement

Hongwei Wang: Writing – original draft, Visualization, Validation, Software, Methodology, Data curation, Conceptualization. **Qiyue Jia:** Conceptualization, Data curation, Methodology, Software, Validation, Writing – original draft. **Yan Wang:** Validation, Methodology, Data curation. **Wenming Xue:** Validation, Data curation. **Qiyue Jiang:** Validation, Data curation. **Fuao Ning:** Validation, Data curation. **Jiaxin Wang:** Validation, Data curation. **Zhonghui Zhu:** Writing – review & editing. **Lin Tian:** Writing – review & editing, Funding acquisition.

Declaration of competing interest

The authors declare that they have no known competing financial interests or personal relationships that could have appeared to influence the work reported in this paper.

References

[1] H. Barnes, N.S.L. Goh, T.L. Leong, R. Hoy, Silica-associated lung disease: an old-world exposure in modern industries, Respirology 24 (2019) 1165–1175, https://doi.org/10.1111/resp.13695.
[2] R.F. Hoy, D.C. Chambers, Silica-related diseases in the modern world, Allergy 75 (2020) 2805–2817, https://doi.org/10.1111/all.14202.
[3] M. Wang, Z. Zhang, J. Liu, M. Song, T. Zhang, Y. Chen, H. Hu, P. Yang, B. Li, X. Song, et al., Gefitinib and fostamatinib target EGFR and SYK to attenuate silicosis: a multi-omics study with drug exploration, Signal Transduct Tar 7 (2022), https://doi.org/10.1038/s41392-022-00959-3.
[4] X.M. Qi, Y. Luo, M.Y. Song, Y. Liu, T. Shu, Y. Liu, J.L. Pang, J. Wang, C. Wang, Pneumoconiosis: current status and future prospects, Chin Med J (Engl) 134 (2021) 898–907, https://doi.org/10.1097/CM9.0000000000001461.
[5] M. Muszynska-Graca, B. Dabkowska, P.Z. Brewczynski, [Guidelines for the use of the International classification of radiographs of pneumoconioses of the international Labour office (ILO): substantial changes in the currrent edition], Med. Pr. 67 (2016) 833–837, https://doi.org/10.13075/mp.5893.00493.
[6] C.C. Leung, I.T.S. Yu, W. Chen, Silicosis, Lancet 379 (2012) 2008–2018, https://doi.org/10.1016/s0140-6736(12)60235-9.
[7] R.F. Hoy, C. Dimitriadis, M. Abramson, D.C. Glass, S. Gwini, F. Hore-Lacy, J. Jimenez-Martin, K. Walker-Bone, M.R. Sim, Prevalence and risk factors for silicosis among a large cohort of stone benchtop industry workers, Occup. Environ. Med. 80 (2023) 439–446, https://doi.org/10.1136/oemed-2023-108892.
[8] K. Newbigin, R. Parsons, D. Deller, R. Edwards, R. McBean, Stonemasons with silicosis: preliminary findings and a warning message from Australia, Respirology 24 (2019) 1220–1221, https://doi.org/10.1111/resp.13672.
[9] E. Meijer, E. Tjoe Nij, T. Kraus, J.S. van der Zee, O. van Delden, M. van Leeuwen, J.W. Lammers, D. Heederik, Pneumoconiosis and emphysema in construction workers: results of HRCT and lung function findings, Occup. Environ. Med. 68 (2011) 542–546, https://doi.org/10.1136/oem.2010.055616.
[10] Y. Wang, F. Cui, X. Ding, Y. Yao, G. Li, G. Gui, F. Shen, B. Li, Automated identification of the preclinical stage of coal workers' pneumoconiosis from digital chest radiography using three-stage cascaded deep learning model, Biomed Signal Proces 83 (2023), https://doi.org/10.1016/j.bspc.2023.104607.
[11] M. Hu, Z. Wang, X. Hu, Y. Wang, G. Wang, H. Ding, M. Bian, High-resolution computed tomography diagnosis of pneumoconiosis complicated with pulmonary tuberculosis based on cascading deep supervision U-Net, Comput. Methods Progr. Biomed. 226 (2022) 107151, https://doi.org/10.1016/j.cmpb.2022.107151.
[12] S. Park, G. Park, S.M. Lee, W. Kim, H. Park, K. Jung, J.B. Seo, Deep learning-based differentiation of invasive adenocarcinomas from preinvasive or minimally invasive lesions among pulmonary subsolid nodules, Eur. Radiol. 31 (2021) 6239–6247, https://doi.org/10.1007/s00330-020-07620-z.
[13] Z. Shi, X. Huang, Z. Cheng, Z. Xu, H. Lin, C. Liu, X. Chen, C. Liu, C. Liang, C. Lu, et al., MRI-Based quantification of intratumoral heterogeneity for predicting treatment response to neoadjuvant chemotherapy in breast cancer, Radiology 308 (2023) e222830, https://doi.org/10.1148/radiol.222830.
[14] D.G. Parr, A. Dirksen, E. Piitulainen, C. Deng, M. Wencker, R.A. Stockley, Exploring the optimum approach to the use of CT densitometry in a randomised placebo-controlled study of augmentation therapy in alpha 1-antitrypsin deficiency, Respir. Res. 10 (2009) 75, https://doi.org/10.1186/1465-9921-10-75.
[15] B.C. Stoel, J. Stolk, Optimization and standardization of lung densitometry in the assessment of pulmonary emphysema, Invest. Radiol. 39 (2004) 681–688.
[16] K. Dekoster, T. Decaesteker, N. Berghen, S. Van den Broucke, A.C. Jonckheere, J. Wouters, A. Krouglov, R. Lories, E. De Langhe, P. Hoet, et al., Longitudinal micro-computed tomography-derived biomarkers quantify non-resolving lung fibrosis in a silicosis mouse model, Sci. Rep. 10 (2020) 16181, https://doi.org/10.1038/s41598-020-73056-6.
[17] T. Li, X. Yang, H. Xu, H. Liu, Early identification, accurate diagnosis, and treatment of silicosis, Cancer Res. J. 2022 (2022) 3769134, https://doi.org/10.1155/2022/3769134.
[18] B. Malengier-Devlies, T. Decaesteker, K. Dekoster, A. Vanstapel, K. Ahmadzadeh, F. Poosti, T. Mitera, L. Seldeslachts, E. Verbeken, C. Wouters, et al., Lung functioning and inflammation in a mouse model of systemic juvenile idiopathic arthritis, Front. Immunol. 12 (2021), https://doi.org/10.3389/fimmu.2021.642778.
[19] L. Mecozzi, M. Mambrini, F. Ruscitti, E. Ferrini, R. Ciccimarra, F. Ravanetti, N. Sverzellati, M. Silva, L. Ruffini, S. Belenkov, et al., In-vivo lung fibrosis staging in a bleomycin-mouse model: a new micro-CT guided densitometric approach, Sci. Rep. 10 (2020) 18735, https://doi.org/10.1038/s41598-020-71293-3.
[20] X. Yang, X.J. Huang, Z. Chen, A.L. Xu, H. Zhou, X.L. Bi, P.Y. Yan, Y. Xie, A novel quantification method of lung fibrosis based on Micro-CT images developed with the optimized pulmonary fibrosis mice model induced by bleomycin, Heliyon 9 (2023) e13598, https://doi.org/10.1016/j.heliyon.2023.e13598.
[21] M. Tsuchiya, T. Masui, K. Terauchi, T. Yamada, M. Katyayama, S. Ichikawa, Y. Noda, S. Goshima, MRI-based radiomics analysis for differentiating phyllodes tumors of the breast from fibroadenomas, Eur. Radiol. 32 (2022) 4090–4100, https://doi.org/10.1007/s00330-021-08510-8.
[22] S. Zhang, J. Wang, S. Sun, Q. Zhang, Y. Zhai, X. Wang, P. Ge, Z. Shi, D. Zhang, CT angiography radiomics combining traditional risk factors to predict brain arteriovenous malformation rupture: a machine learning, multicenter study, Transl Stroke Res (2023), https://doi.org/10.1007/s12975-023-01166-0.
[23] S. Zhao, J. Wang, C. Jin, X. Zhang, C. Xue, R. Zhou, Y. Zhong, Y. Liu, X. He, Y. Zhou, et al., Stacking ensemble learning-based [(18)F]FDG PET radiomics for outcome prediction in diffuse large B-cell lymphoma, J. Nucl. Med. (2023), https://doi.org/10.2967/jnumed.122.265244.
[24] J. Zhao, Q. Jiang, C. Xu, Q. Jia, H. Wang, W. Xue, Y. Wang, Z. Zhu, L. Tian, MiR-26a-5p from HucMSC-derived extracellular vesicles inhibits epithelial mesenchymal transition by targeting Adam17 in silica-induced lung fibrosis, Ecotoxicol. Environ. Saf. 257 (2023) 114950, https://doi.org/10.1016/j.ecoenv.2023.114950.
[25] M. Yang, D. Wang, S. Gan, B. Wang, L. Yu, Y. Xie, L. Fan, J. Ma, W. Chen, Triiodothyronine ameliorates silica-induced pulmonary inflammation and fibrosis in mice, Sci. Total Environ. 790 (2021) 148041, https://doi.org/10.1016/j.scitotenv.2021.148041.
[26] Q. Zhou, Y. Guan, R. Hou, J. Wang, H. Gao, H. Li, Y. Zhao, N. Liu, Y. Wang, N. Li, S. Yao, PolyG mitigates silica-induced pulmonary fibrosis by inhibiting nucleolin and regulating DNA damage repair pathway, Biomed. Pharmacother. 125 (2020) 109953, https://doi.org/10.1016/j.biopha.2020.109953.
[27] D. Cheng, Q. Xu, Y. Wang, G. Li, W. Sun, D. Ma, S. Zhou, Y. Liu, L. Han, C. Ni, Metformin attenuates silica-induced pulmonary fibrosis via AMPK signaling, J. Transl. Med. 19 (2021) 349, https://doi.org/10.1186/s12967-021-03036-5.
[28] F. Cassol, L. Portal, S. Richelme, M. Dupont, Y. Boursier, M. Arechederra, N. Auphan-Anezin, L. Chasson, C. Laprie, S. Fernandez, et al., Tracking dynamics of spontaneous tumors in mice using photon-counting computed tomography, iScience 21 (2019) 68–83, https://doi.org/10.1016/j.isci.2019.10.015.
[29] X. Artaechevarria, D. Blanco, D. Perez-Martin, G. de Biurrun, L.M. Montuenga, J.P. de Torres, J.J. Zulueta, G. Bastarrika, A. Munoz-Barrutia, C. Ortiz-de-Solorzano, Longitudinal study of a mouse model of chronic pulmonary inflammation using breath hold gated micro-CT, Eur. Radiol. 20 (2010) 2600–2608, https://doi.org/10.1007/s00330-010-1853-0.

[30] J. Li, R. Zuo, U.J. Schoepf, J.P. Griffith, S. Wu, C. Zhou, X. Chen, W. Tan, Z. Zhou, H. Gao, et al., Development and validation of a nonenhanced CT based radiomics model to detect brown adipose tissue, Theranostics 13 (2023) 1584–1593, https://doi.org/10.7150/thno.81789.
[31] T. Yang, Y. Ying, AUC maximization in the era of big data and ai: a survey, ACM Comput. Surv. 55 (2022) 1–37, https://doi.org/10.1145/3554729.
[32] H. Saleh, S. Mostafa, A. Alharbi, S. El-Sappagh, T. Alkhalifah, Heterogeneous ensemble deep learning model for enhanced Arabic sentiment analysis, Sensors 22 (2022), https://doi.org/10.3390/s22103707.
[33] C. Cavalin, A. Lescoat, A. Ballerie, N. Belhomme, P. Jego, S. Jouneau, V. Lecureur, M. Lederlin, C. Paris, P.A. Rosental, Beyond silicosis, is the world failing on silica hazards? Lancet Respir. Med. 7 (2019) 649–650, https://doi.org/10.1016/S2213-2600(19)30174-2.
[34] M. The Lancet Respiratory, The world is failing on silicosis, Lancet Respir. Med. 7 (2019) 283, https://doi.org/10.1016/S2213-2600(19)30078-5.
[35] M. Mascalchi, G. Camiciottoli, S. Diciotti, Lung densitometry: why, how and when, J. Thorac. Dis. 9 (2017) 3319–3345, https://doi.org/10.21037/jtd.2017.08.17.
[36] E.F. Redente, K.W. Kopf, A.N. Bahadur, A. Robichaud, L.K. Lundblad, L.T. McDonald, Application-specific approaches to MicroCT for evaluation of mouse models of pulmonary disease, PLoS One 18 (2023) e0281452, https://doi.org/10.1371/journal.pone.0281452.
[37] J.C. Cooley, N. Javkhlan, J.A. Wilson, D.G. Foster, B.L. Edelman, L.A. Ortiz, D.A. Schwartz, D.W. Riches, E.F. Redente, Inhibition of antiapoptotic BCL-2 proteins with ABT-263 induces fibroblast apoptosis, reversing persistent pulmonary fibrosis, JCI Insight 8 (2023), https://doi.org/10.1172/jci.insight.163762.
[38] Z. Peng, M. Duan, Y. Tang, J. Wu, K. Zhao, Y. Zhong, Z. He, J. Meng, F. Chen, X. Xiao, et al., Impaired interferon-gamma signaling promotes the development of silicosis, iScience 25 (2022) 104647, https://doi.org/10.1016/j.isci.2022.104647.
[39] F. Pennati, L. Leo, E. Ferrini, N. Sverzellati, D. Bernardi, F.F. Stellari, A. Aliverti, Micro-CT-derived ventilation biomarkers for the longitudinal assessment of pathology and response to therapy in a mouse model of lung fibrosis, Sci. Rep. 13 (2023) 4462, https://doi.org/10.1038/s41598-023-30402-8.
[40] M. Buccardi, E. Ferrini, F. Pennati, E. Vincenzi, R.E. Ledda, A. Grandi, D. Buseghin, G. Villetti, N. Sverzellati, A. Aliverti, F.F. Stellari, A fully automated micro-CT deep learning approach for precision preclinical investigation of lung fibrosis progression and response to therapy, Respir. Res. 24 (2023) 126, https://doi.org/10.1186/s12931-023-02432-3.
[41] D.R. McIlrath, E. Roach, G. Porro, C.J. Perez-Torres, Feasibility of quantification of murine radiation-induced pulmonary fibrosis with microCT imaging, J. Radiat. Res. (2021), https://doi.org/10.1093/jrr/rrab096.
[42] D. De Ruysscher, P.V. Granton, N.G. Lieuwes, S. van Hoof, L. Wollin, B. Weynand, A.M. Dingemans, F. Verhaegen, L. Dubois, Nintedanib reduces radiation-induced microscopic lung fibrosis but this cannot be monitored by CT imaging: a preclinical study with a high precision image-guided irradiator, Radiother. Oncol. 124 (2017) 482–487, https://doi.org/10.1016/j.radonc.2017.07.014.
[43] M. Nakagawa, T. Nakaura, T. Namimoto, Y. Iyama, M. Kidoh, K. Hirata, Y. Nagayama, H. Yuki, S. Oda, D. Utsunomiya, Y. Yamashita, Machine learning to differentiate T2-weighted hyperintense uterine leiomyomas from uterine sarcomas by utilizing multiparametric magnetic resonance quantitative imaging features, Acad. Radiol. 26 (2019) 1390–1399, https://doi.org/10.1016/j.acra.2018.11.014.
[44] S.K. Kalagotla, S.V. Gangashetty, K. Giridhar, A novel stacking technique for prediction of diabetes, Comput. Biol. Med. 135 (2021) 104554, https://doi.org/10.1016/j.compbiomed.2021.104554.
[45] J. Liu, X. Dong, H. Zhao, Y. Tian, Predictive classifier for cardiovascular disease based on stacking model fusion, Processes 10 (2022), https://doi.org/10.3390/pr10040749.